Inorganic Chemistry

Article

pubs.acs.org/IC

Room-Temperature Synthesis of Iron-Doped Anatase TiO_2 for Lithium-Ion Batteries and Photocatalysis

Christian Andriamiadamanana,[†,‡,§] Christel Laberty-Robert,[‡,§] Moulay T. Sougrati,[§,∥] Sandra Casale,[⊥] Carine Davoisne,[†,§] Snehangshu Patra,[†,§] and Frédéric Sauvage*[,†,§]

[†]Laboratoire de Réactivité et Chimie des Solides, CNRS UMR 7314, Université de Picardie Jules Verne, 33 rue Saint-Leu, 80039 Amiens Cedex, France

[‡]Laboratoire de Chimie de la Matière Condensée de Paris, CNRS UMR 7574, Université Pierre et Marie Curie (Paris VI), Collège de France, Bâtiment C−D, 11 place Marcelin-Berthelot, 75231 Paris, France

[§]Réseau sur le Stockage Electrochimique de l'Energie, CNRS FR3459, 80039 Amiens Cedex, France

[∥]Institut Charles Gerhardt, CNRS UMR 5253, CC004, Université Montpellier 2, 34095 Montpellier Cedex 5, France

[⊥]Laboratoire de Réactivité de Surface, CNRS UMR 7197, 4 Place Jussieu, F-75005 Paris, France

Supporting Information

ABSTRACT: Iron-doped nanocrystalline particles of anatase TiO_2 (denoted *x*% Fe-TiO_2, with *x* the nominal [Fe] atom % in solution) have been successfully synthesized at room temperature by a controlled two-step process. Hydrolysis of titanium isopropoxide is first achieved to precipitate $Ti(OH)_4$ species. A fine control of the pH allows one to maintain (i) soluble iron species and (ii) a sluggish solubility of $Ti(OH)_4$ to promote a dissolution and condensation of titanium clusters incorporating iron, leading to the precipitation of iron-doped anatase TiO_2. The pH does then influence both the nature and crystallinity of the final phase. After 2 months of aging at pH = 2, well-dispersed nanocrystalline iron-doped TiO_2 particles have been achieved, leading to 5−6 nm particle size and offering a high surface area of ca. 280 m^2/g. This dissolution/recrystallization process allows the incorporation of a dopant concentration of up to 7.7 atom %; the successful incorporation of iron in the structure is demonstrated by X-ray diffraction, high-resolution transmission electron microscopy, and Mössbauer spectroscopy. This entails optical-band-gap narrowing from 3.05 to 2.30 eV. The pros and cons effects of doping on the electrochemical properties of TiO_2 versus lithium are herein discussed. We reveal that doping improves the power rate capability of the electrode but, in turn, deserves the electrolyte stability, leading to early formation of SEI. Finally, we highlight a beneficial effect of low iron introduction into the anatase lattice for photocatalytic applications under standard AM1.5G visible-light illumination.

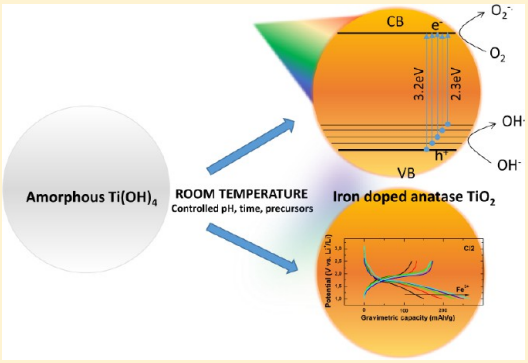

INTRODUCTION

Although the development of new materials and new technologies is mainly focused on the improvement of their performances, less concern is inscribed in the development of more ecofriendly and low-cost synthetic procedures. Among parameters affecting costs and the environmental footprint, the temperature of synthesis appears to be one of the most important. Up to now, effective synthesis at room temperature remains complicated and probably not versatile to all existing systems. During the last years, only a few counterexamples appeared in the literature showing the possibility to synthesize more or less complicated structures with excellent crystallinity, under a procedure led entirely at room temperature.[1−4] However, besides these examples, no synthesis of doped materials at room temperature has ever been reported in spite of the numerous advantages that it can bring in several domains such as energy storage to enhance the power capability of the initial electrode[5] and photocatalysis to pave the way to visible-light excitation,[6] which are the two applications targeted for the materials reported here.

TiO_2 is probably one of the most studied oxide semiconductor materials. It is used in a broad range of applications such as cosmetics,[7] paints,[8] (photo)catalysis,[9] photovoltaic and hybrid light-emitting diodes,[10] and, as aforementioned, alkali-ion batteries.[11] One reason to explain this interest for TiO_2 stems from both its polymorphism richness and its $3d^0$ electronic configuration inducing exceptional sensitiveness of the optoelectronic properties to the introduction of point defects. This is the unique oxide semiconductor for which the band-gap energy can be manipulated not only from a white 3.2 eV value (ca. 390 nm) to a black 1.5 eV value (ca. 830 nm)[12,13] but also inversely blue-shifted to 3.8 eV (ca. 325 nm) as a result of the quantum confinement effect.[14] For these reasons, TiO_2 is

Received: May 7, 2014
Published: September 11, 2014

   dx.doi.org/10.1021/ic501067p | Inorg. Chem. 2014, 53, 10129−10139

among the best candidates for our study, which aims at the doping at room temperature and characterization of its performance.

Room-temperature synthesis offers control in the nucleation and growth processes, leading, in the case of TiO_2, to nanocrystalline powders exhibiting a very high surface area of 300 m^2/g. This high surface area promotes the surface reactivity vis-à-vis of the volume entailing a crossover in the lithium insertion mechanism from a two-phase reaction to a complete solid−solution domain.[15−18]

The novelty of this work relies on a first example showing the feasibility to tailor, under room-temperature conditions, aliovalent doping of TiO_2 by means of Fe^{3+}. Against the general preconceived idea that heating is required to obtain crystallized materials and for doping, we herein highlight that the substantial incorporation of dopant can be achieved as a result of a dissolution/recrystallization process. The interest for Fe^{3+} stems from its ability to modify substantially the optoelectronic properties of anatase TiO_2 and on its ionic radii compared to Ti^{4+} ($r_{Fe^{3+}}$ = 0.645 Å vs $r_{Ti^{4+}}$ = 0.605 Å).[19] This achievement was performed using the appropriate pH and time conditions to allow condensation of both iron and titanium clusters, leading to well-crystallized 5 nm anatase particles attaining up to 280 m^2/g. As a result of the acceptor point defect created by the inclusion of Fe^{3+}, the material's absorption shifts toward the visible range to a band gap of ca. 2.3 eV. Such characteristics make these materials appealing for applications in lithium-ion batteries and photocatalysis, for which their performances will be discussed to assess the real outcome of doping the original anatase TiO_2.

EXPERIMENTAL SECTION

Synthesis. *x* Fe-doped TiO_2 (with *x* = 0, 0.5, 1, 2.5, and 5 atom %) were synthesized at room-temperature conditions according to a modified two-step procedure.[15] The first step aims at hydrolysis of titanium(IV) isopropoxide [$Ti(OiPr)_4$; Sigma-Aldrich]. Typically, 1 volume of $Ti(OiPr)_4$ is added stepwise to 10 volumes of deionized water under constant magnetic stirring, leading instantaneously to the formation of a white precipitate. Hydrolysis is left for 2 h for completion. The precipitate is retrieved by centrifugation and washed several times with water and a last time with ethanol before drying at room temperature. This amorphous intermediate is then aged in an aqueous acidic solution, for which the pH is controlled by the addition of H_2SO_4 after having introduced the amorphous titania.

For doping, $FeCl_3$ (98%, Redel de Haën) was incorporated into this acidic solution in various ratios (Fe^{3+}/Ti^{4+} ratio = 0/100, 0.5/99.5, 1/99, 2.5/97.5, 5/95). Typically, 1 g of the as-synthesized powder is poured in 10 mL of aging solution containing the appropriate amount of Fe^{3+} for 60 days. The final product is also retrieved by centrifugation using a procedure similar to that described above.

Characterization. The Brunauer−Emmett−Teller (BET) surface area and pore-size distribution using the Barrett−Joyner−Halenda method were evaluated by N_2 physisorption at 77 K using a Micrometrics ASAP 2020 analyzer. Prior to analysis, the samples were first degassed under vacuum (5 μmHg) at 303 K for 1 h, then heated at a rate of 5 K/min to 393 K, and held at this temperature for 3 h.

Thermogravimetric analysis coupled with mass spectrometry was recorded using a Netzsch STA 449 C Jupiter instrument. Analysis was performed from room temperature to 600 °C under air at a heating rate of 5 °C/min. X-ray diffraction (XRD) analysis was carried out using a Bruker D4 ENDEAVOR diffractometer with a Cu Kα source.

High-resolution transmission electron microscopy (HRTEM) experiments were carried out using either a JEOL JEM 2011 LaB_6 microscope operating at 200 kV or a FEI Tecnai F20 S-TWIN (FEG) operating at 200 kV for analysis of air-sensitive electrodes. Air-sensitive samples were prepared in an argon-filled glovebox and transferred to a transmission electron microscope without any air exposure.

^{57}Fe Mössbauer spectra were measured using a ^{57}Co source in rhodium metal. Absorbers are made of 250 mg of powder mixed with boron nitride as the binder. The measurements were conducted either at ambient temperature (295 K) or at liquid-nitrogen temperature (77 K). In all experiments, the source was kept at ambient temperature. The spectrometer was operated with a triangular velocity waveform. A NaI scintillation detector was used for γ-ray collection. The spectra were fitted with the appropriate superposition of Lorentzian lines using PC-Mos II computer software.

The band-gap value was determined using a Jobin Yvon Cary UV−vis−near-IR spectrometer on samples pressed into pellets. For this, diffuse-reflectance mode using an integrating sphere was used and the value determined using Kubelka−Munk formalism.[20]

The iron content cell was determined by inductively coupled plasma atomic emission spectroscopy (ICP-AES) using a Thermo Scientific iCAP 6000 series ICP spectrophotometer. For this, the powders were dissolved in a concentrated H_3PO_4 aqueous solution (85%) at 60 °C and subsequently diluted before analysis. The measurements were set at 238 and 204 nm wavelengths for iron and at 323 and 452 nm wavelengths for titanium detection, respectively.

Galvanostatic measurements were carried out using a Swagelok-type cell. The active material was mixed in a mortar with 17.6% commercial Ketjen Black carbon KB600 (Akzonobel). The cell was typically loaded with ca. 10 mg/cm^2 of composite. The experiments were done on a two-electrode configuration where both the counter electrode and reference electrode are composed of a lithium metal foil (Aldrich). The two electrodes are separated by two Whatman GF/D borosilicate glass fiber sheets soaked with LP30 Merck electrolyte (1 mol/L $LiPF_6$ in a 1:1 volume ratio of ethylene carbonate and dimethyl carbonate). The electrochemical cells were assembled inside an argon-filled glovebox with O_2 and H_2O under the 0.1 ppm level. The electrochemical measurements were conducted using a Biologic multichannel VMP galvanostat/potentiostat.

Photocatalytic degradation of rhodamine B (RhB, [9-(2-carboxyphenyl)-6-(diethylamino)-3-xanthenylidene]diethylammonium chloride) was investigated by dispersing 100 mg of the semiconductor in 100 mL of an aqueous solution containing RhB, whose concentration was adjusted to obtain an optical density of 2.0. The dispersion was magnetically stirred in the dark for 30 min before measurements. For time-dependent measurements, 3 mL of the sample was taken up, kept under dark using aluminum foil, and centrifuged. The xenon white light source used is a Newport 3A quality solar simulator adjusted to AM1.5G condition (ϕ = 100 mW/cm^2). The absorbance of the resulting solution was measured by UV−vis spectrometry using a Jasco V-630 spectrophotometer.

RESULTS AND DISCUSSION

Room-Temperature Synthesis and Characterization of *x* Fe-Doped TiO_2 (with *x* = 0, 0.5, 1, 2.5, and 5 atom %). To achieve the room-temperature synthesis of Fe-doped TiO_2, it requires optimization of the chemical bath in terms of the nature of the precursors, relative concentration, and pH, which together will determine the nature of species present in solution. Recently, a two-step synthetic procedure was optimized to obtain 4-nm-size anatase TiO_2 at room temperature.[15] The first step is nested in hydrolysis of titanium alkoxide followed by aging in an aqueous solution of 0.1 mol/L NH_4F(aq) to crystallize anatase TiO_2 (uncontrolled pH). By slightly adapting this first procedure while getting rid of the fluoride precursor and carefully controlling the pH of the aging solution, we gathered the powder XRD patterns collected after 60 days of aging in an acidic solution at room temperature without dopant (Figure 1a).

For pH = 1, the as-synthesized powder is composed of the two most common allotropic forms of TiO_2, anatase and rutile,

dx.doi.org/10.1021/ic501067p | Inorg. Chem. 2014, 53, 10129−10139

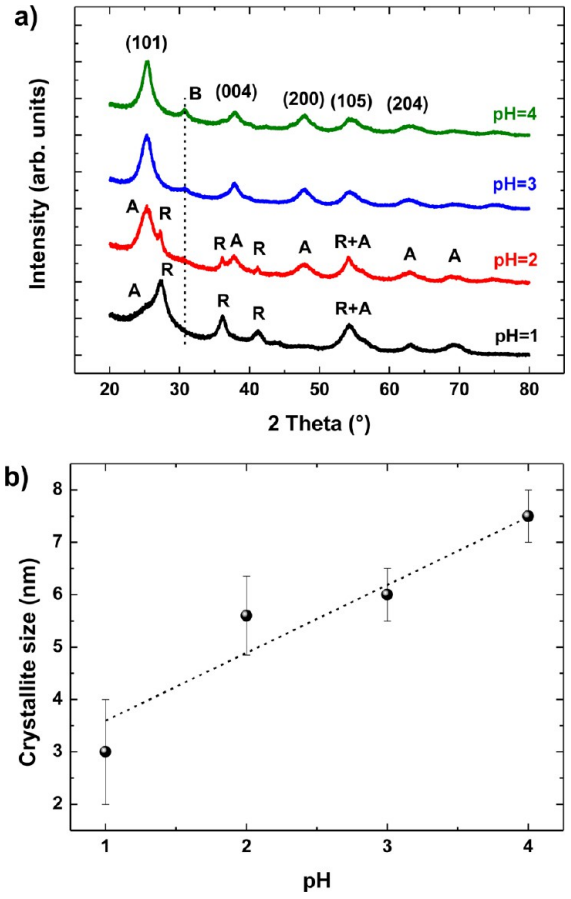

Figure 1. (a) X-ray diffractogram of the powder retrieved after 60 days of aging of $Ti(OH)_4$ at room temperature in different pH solutions. (b) Corresponding crystallite size measured using the Scherrer equation.

with the latter being the major phase (78%). Note that the ratio between the two forms was determined using the empirical method proposed by Spurr and Meyers.[21] The preferential formation of rutile is not surprising because it corresponds to the thermodynamically most stable TiO_2 polymorph. It is therefore the typical structure obtained for the Ostwald ripening mechanism.[22]

For higher pH, the quantity of rutile decreases. At pH = 2, the anatase overrides the rutile (72% anatase), and for pH > 2, the rutile is no longer formed. A small peak appears at 2θ = 30.6° corresponding to traces of brookite, with the latter getting promoted with further increases of the pH. The effect of the pH on the final product stresses both the impact of the solubility of hydrolyzed titanium on the allotrope formed and the ionic strength of the medium on the condensation process. At low pH, rutile formation is common during hydrothermolysis at conditions where crystallization of TiO_2 takes place according to a sluggish dissolution/precipitation mechanism.[23]

Evolution of the crystallite size as a function of the pH has been determined by using the semi-empirical Scherrer equation on the most intense (101) diffraction plane (Figure 1b). Interestingly, a linear relationship between the crystallite size and solution pH is observed from 3 (±1) to 7.5 (±0.5) nm at pH = 4. This evolution suggests that nucleation versus growth is favored at low pH or alternatively that the condensation rate gets slowed down. This, in turn, explains again the preferential crystallization of the rutile at low pH because it is the thermodynamically stable phase. This feature has been discussed by Gopal et al., who have shown that the anatase can be favored provided that the polycondensation rate gets faster,[24] and discussed by Suggimoto et al. in terms that the nucleation rate leading to the anatase is governed by the concentration of $Ti(OH)_3^+$.[25] The condensation rate can be endorsed, for instance, by increasing the temperature to 60 °C, which gives the anatase in good agreement (Figure S1 in the Supporting Information, SI). Note that thermolysis at 60 °C enables one to shorten the aging time to 7 days. We also verify a linear relationship between the pH and crystallite size from 5.3 (±0.5) to 7.7 (±0.5) nm. Note that the use of sulfuric acid to adjust the pH was chosen deliberately to direct the anatase structure because it was shown that chloride and oxalate favor the formation of brookite and rutile, respectively.[26]

The aging time affects the crystallinity of the resulting powder. For pH = 2, the as-synthesized component after 17 days of aging is already crystallized based on XRD with no further evolution of the crystallite size (ca. 5.5 nm; Figure S2 in the SI). However, TEM investigations reveal that, after 30 days, the material remains a mixture of crystalline anatase TiO_2 and the amorphous part surrounding the crystallized region, as indicated by the arrows in Figure 2a. After 60 days of aging, no more amorphous parts were noticed (Figure 2b). The particles exhibit spheroidal morphology, whose size is in excellent agreement with the crystallite size determined by XRD, thus indicating that particles are, in fact, single crystals (Figure 2a,b).

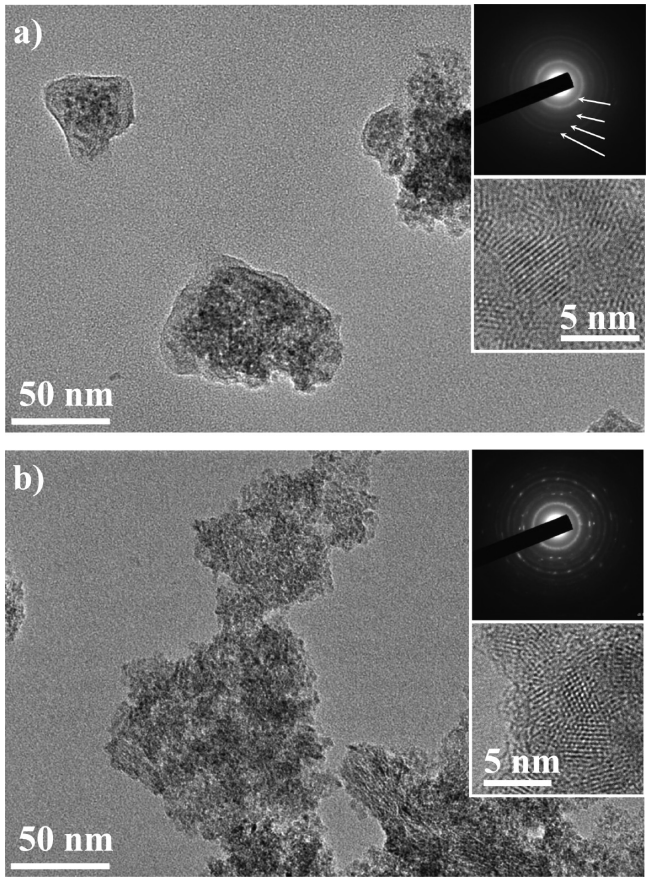

Figure 2. TEM images of samples retrieved (a) after 30 and (b) 60 days of aging at pH = 2.

dx.doi.org/10.1021/ic501067p | *Inorg. Chem.* 2014, 53, 10129−10139

When Fe^{3+} is introduced to the aging solution, control of the pH becomes crucial to avoid the precipitation of iron hydroxide or oxyhydroxide while maintaining slow solubility of titanium hydroxide to be able to incorporate Fe^{3+} during the condensation process. Sugimito et al. reported the speciation diagram of Ti^{4+} in an aqueous solution, pointing out the onset of zero charge precursors appearing at pH > 2.[27] Similarly, Stefansson reported the one corresponding to Fe^{3+} determining the stability of $Fe(OH)_3$ species at pH between 6 and 10.[28] Accordingly, iron hydroxide precipitation is avoided by fixing the aging solution pH far from 6 while not being too close to the maximum stability domain of $Ti(OH)_4$ species. Considering these two factors, the optimal pH to dope TiO_2 by Fe^{3+} would be around 2. At this value, $Ti(OH)_4$ exhibits a sluggish solubility, leading to an equilibrium reaction between two different charge species in the same proportion, $Ti(OH)_3^+$ and $Ti(OH)_2^{2+}$, and Fe^{3+} species in the forms of soluble Fe^{3+}, $Fe(OH)^{2+}$, and $Fe(OH)_2^+$.[29] Note that the stability of Fe^{3+} species in an aqueous solution of pH = 2 was separately verified in the absence of a titanium precursor for which no precipitate was observed until 3 months. The iron concentration was varied from 0, 0.5, 1, 2.5, to 5 atom %. The XRD pattern recorded for the different resulting samples is given in Figure 3a. First, the addition of Fe^{3+} in the aging solution hampers rutile formation. Regardless of the iron concentration, the final product has an invariable crystallite size between 5 and 6 nm (Figure 3b). When the powder is heated in air (Figure S3a in the SI), the iron-doped anatase TiO_2 starts to convert in rutile at 500 °C and completely at 600 °C. Interestingly, the thermal stability domain of the rutile is particularly narrow because from 700 °C it turns directly to the pseudo-brookite-like structure Fe_2TiO_5. This thermal behavior of the doped sample is noticeably different from that of the undoped counterpart, which typically undergoes only one transition from anatase to rutile at 710 °C (Figure S3b in the SI). Such a difference in the thermal stability stems from doping. Indeed, it is now well-established that the incorporation of aliovalent dopant in the anatase structure drastically modifies the thermal activation energy for the rutile transition.[30−32] It also explains the formation of the pseudo-brookite Fe_2TiO_5, which is never formed from a separate solid-state reaction between $Fe(OH)_3$ and $Ti(OH)_4$.

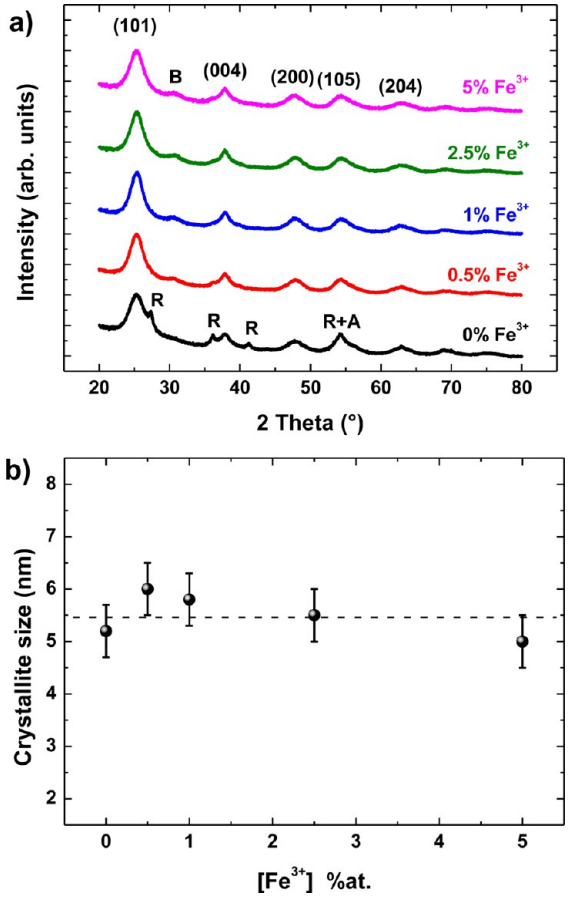

Figure 3. (a) X-ray diffractogram of samples with different iron concentrations after 60 days of aging at pH = 2. (b) Corresponding crystallite size measured using the Scherrer equation.

The incorporation of Fe^{3+} seems to accelerate the crystallization process if we compare the selected area electron diffraction (SAED) patterns after 30 days of aging. The doped material shows greater crystallinity than the undoped counterpart. This is an interesting observation because it tends to account once again for the preferential formation of anatase upon the addition of iron; faster crystallization leads preferentially to anatase for kinetic reasons as discussed above.

The introduction of Fe^{3+} into the lattice creates crystallographic and electronic point defects.[33] Iron preferentially substitutes for titanium. The extra hole charge is compensated by the formation of a half-oxygen vacancy.[34]

$$Fe^{3+}_{solvated} + Ti^{x}_{Ti} \rightarrow \left[Fe_{Ti}{}' + \frac{1}{2}V_{\ddot{O}} \right]_{TiO_2}$$

The nanocrystalline state of our particles impedes any Rietveld refinement to locate the exact position of Fe^{3+} in the lattice or at least to verify Vegard's law. Nevertheless, the successful introduction of Fe^{3+} into the crystal is confirmed by Mössbauer spectroscopy. At 295 K, no sextet feature was observed, showing the absence of supermagnetic hematite α-Fe_2O_3 in the sample. The spectrum is only composed of a doublet, for which the hyperfine parameters are characteristic of Fe^{3+} in a high-spin configuration (Figure 4a). The isomeric shift of 0.38 mm/s and the quadrupole splitting of 0.53 mm/s are typical for Fe^{3+} in an FeO_6-type octahedral site. These values are also in excellent agreement with the numbers previously reported for iron-doped anatase TiO_2 (Table 1).[35−37] The high value of the line width (0.52 mm/s) is ascribed to the nanosize of the particles. Note that the spectrum is not changed at liquid-nitrogen temperature (Figure 4b).

The evolution of the BET surface area and pore-size distribution for both TiO_2 and Fe-doped TiO_2 is summarized in Table 2 and shown in Figure 5. According to the IUPAC recommendation, all samples showed type IV adsorption isotherms with a combination of H2 and H4 hysteresis, indicating the simultaneous presence of mesopores and micropores. The value of the BET surface area for the undoped sample is about 230 m^2/g for a mean monomodal pore size of 5.1 nm. For doping, the BET value varies between 260 and 280 m^2/g and the pore size decreases, first to 4.5 nm before separating into a bimodal distribution for a greater doping level than 0.5%. TEM micrographs depict that the undoped sample is composed of highly agglomerated particles. On the contrary, the doped samples look better dispersed (Figure 6). For 2.5% and 5% Fe^{3+} doping, the two samples appear free of aggregates, with primary particles displaying a rocklike morphology.

dx.doi.org/10.1021/ic501067p | Inorg. Chem. 2014, 53, 10129−10139

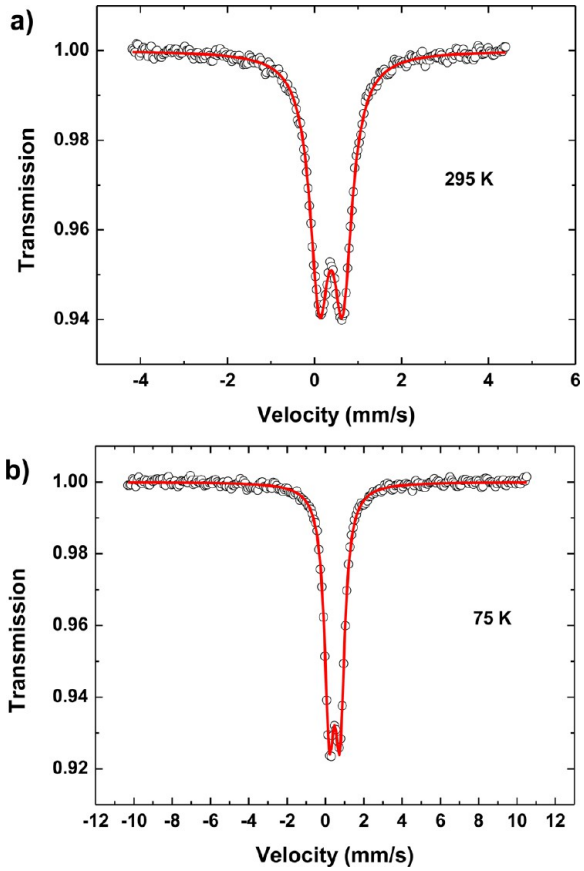

Figure 4. Mössbauer spectra of the 5% Fe^{3+}-doped TiO_2 recorded at (a) 295 and (b) 75 K.

Table 1. Mössbauer Parameters Corresponding to the Spectra Reported in Figure 4[a]

T (K)	IS (mm/s)	QS (mm/s)	LW (mm/s)
295	0.38	0.53	0.52
77	0.48	0.55	0.61

[a]IS, QS, and LW correspond to the isomeric shift, the quadrupole splitting, and the line width, respectively. The isomer shift is given relative to the α-Fe standard at room temperature.

Table 2. Evolution of the BET Surface Area and Pore Size as a Function of the Doping Concentration Introduced in an Aging Solution

Fe concn (atom %)	BET surface area (m^2/g)	pore size (nm)
0	235	5.1
0.5	261	4.7
1	268	3.8
2.5	282	4/5.2
5	260	4/4.8

The precise Fe^{3+} content successfully incorporated has been determined by combining energy-dispersive X-ray (EDX) spectroscopy and ICP-AES analysis. These two techniques give very comparable numbers, which are tabulated (cf. Table 3). There is only a discrepancy between the two techniques for the 0.5% sample, which can be attributed to the known lack of EDX sensitiveness at an atomic level below 1%. In a very reproducible way, the amount of iron incorporated in the solid is systematically greater than the amount introduced in solution. Although surprising at first sight, this feature emphasizes the dissolution/recrystallization mechanism proposed. In this case, the amount of titanium recrystallized with respect to the amount solubilized is not quantitative in yield, namely, a certain concentration of titanium cation remains in solution without precipitating.

An important outcome resulting from the doping of TiO_2 concerns the shift of the absorption toward visible light. For doping with iron, a modification of color is observed from the typical white color for TiO_2 to orange, with coloration intensifying with the content of iron. This color evolution is ascribed to the absorption edge shifting toward lower energies from 3.05 eV for the undoped material to 2.9, 2.75, 2.4, and 2.3 eV for the 0.5%, 1%, 2.5%, and 5% Fe^{3+}-doped TiO_2, respectively (Figure 7a,b). These values are in good agreement with the values reported in the literature for iron-doped TiO_2 synthesized by thermolysis or hydrosolvothermal or radio-frequency thermal plasma.[38−40] Note that the band-gap value of the undoped TiO_2 sample synthesized by means of this room-temperature approach lies slightly below the value typically encountered (i.e., 3.2 eV). This change can be ascribed to a slight oxygen substoichiometry triggered by the long duration of aging in acidic media used for the synthesis, which causes energy destabilization of the valence band.[41] We note also the presence of an absorption feature at 2.6 eV. Basically, three types of transitions can be observed in the UV−vis spectra of Fe^{3+}: ligand-field transitions, ligand-to-metal charge-transfer transitions, and transitions resulting from the simultaneous excitation of magnetically coupled Fe^{3+}. This coupling can occur between two Fe^{3+} but also between Fe^{3+} and another cation.[42] The absorption feature at 2.6 eV is likely ascribed to this last transition.

Applications. *a. Lithium Battery Performance Studies.* The lithium insertion/deinsertion properties were evaluated versus lithium metal at *C*/2, *C*/20, and *C*/50 rates. Figure 8 shows the first cycle galvanostatic discharge/charge profile for undoped TiO_2 prepared at pH = 2 (anatase + rutile mixture) and undoped TiO_2 synthesized at pH = 3 (pure anatase), both used as a reference material and compared to iron-doped samples. Note that, first, the small textural modifications induced by dopant inclusion have no or only a very minor effect on the electrochemical properties. Second, the undoped sample prepared at pH = 3 (pure anatase) shows better electrochemical performances versus lithium than the sample prepared at pH = 2, which contains rutile as part of the anatase. We remind everyone that the rutile counterpart is known to exhibit poorer electrochemical activity versus lithium especially at high cycling rates, which for compensation requires careful downsizing toward the nanoscale.[43] The difference in the capacity between these two comes less blatantly at lower rates as a result of the higher kinetic limitations in the denser rutile polymorph (Figure 8b,c).

Lithium insertion into nano-TiO_2 enlists three main steps. The first one depicts a rapid drop of the potential to ca. 1.7 V (vs Li^+/Li) characteristic of a solid−solution domain for which the composition (ε) strongly depends on the particle size.[16,44] This step precedes a voltage−composition plateau at around 1.7 V involving a two-phase reaction between the tetragonal $Li_\varepsilon TiO_2$ and orthorhombic lithium titanate $Li_{0.5\pm\delta}TiO_2$ (space group *Imma*).[45] As for ε, the value of δ also strongly relies on the particle size and synthetic conditions.[7,15] After the plateau, another two-phase reaction takes place up to 1 V between $Li_{0.5\pm\delta}TiO_2$ and a rock-salt-type tetragonal $Li_{1.0}TiO_2$.[46] The

dx.doi.org/10.1021/ic501067p | Inorg. Chem. 2014, 53, 10129−10139

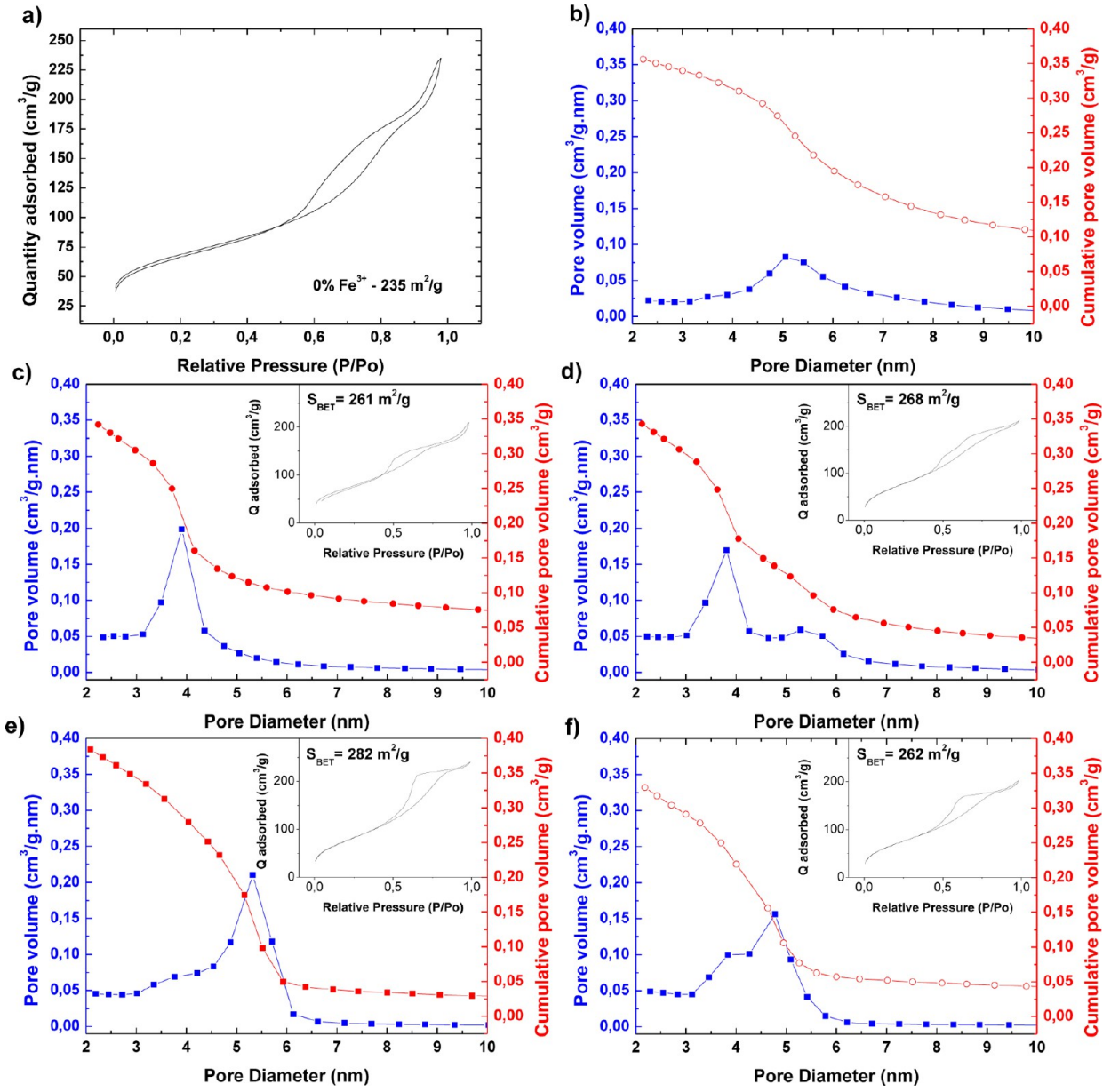

Figure 5. N_2 physisorption isotherms and corresponding pore-size distributions of room-temperature-synthesized particles with different Fe^{3+} concentrations of (a and b) 0, (c) 0.5, (d) 1, (e) 2.5, and (f) 5% Fe^{3+}-doped samples.

poor electrochemical reversibility of the latter has for long-term constraints an inferior cutoff potential up to 1.5 V versus Li^+/Li. Recent progress on the nanostructuration of TiO_2 has induced noticeable reversibility improvement in this composition range.[17] We evaluated the solid−solution domain to an extent of ca. 0.11 Li^+ for the undoped TiO_2 at $C/20$. At a lower regime ($C/50$), in the first portion of the discharge, all samples show good overlay, indicating that iron inclusion in the lattice has no effect on the extent of this lithium solid solution. By contrast, a slight difference is experienced at higher regimes, which likely accounts for improved kinetics for doping of the anatase by iron (Figure 8a,b). This is also observed upon comparison of the first cycle discharge capacity. The latter increases with the doping level from 150 to ca. 270 mAh/g at $C/2$. The discharge capacity at the lower regimes attains ca. 320 mAh/g, which is close to the theoretical value of 335 mAh/g for $Li_{1.0}TiO_2$. For doping, this theoretical capacity value is largely exceeded. Indeed, the discharged capacity obtained at $C/50$ would correspond to the insertion of 1.16, 1.33, and 1.65 Li^+ for 1, 2.5, and 5% doping levels, respectively. This observation of extracapacities reproduces well the results recently published by Das et al.[47] These authors have ascribed this phenomenon for modification of TiO_2 with iron to a doping effect favoring the onset of a conversion reaction, a mechanism elucidated by Poizot et al. in ref48. Our results disagree nonetheless with the recent report published by Hutchings et al. showing that iron doping has no benefit by contrast to nickel and cobalt doping;[49] albeit important textural modifications between the reference and doped materials render the real intrinsic effect of doping misleading. Note that in our case the BET surface area discrepancy lies below 20%, a value that should not noticeably impact the electrochemical behavior because the particle size discrepancies will be around or less than 1 nm. The improvement of the rate capability for doping of the anatase TiO_2 by iron cannot be related to a drastic enhancement of the conductivity. Indeed, Chandiran et al.[32] and Djenizian et al.[50]

dx.doi.org/10.1021/ic501067p | Inorg. Chem. 2014, 53, 10129−10139

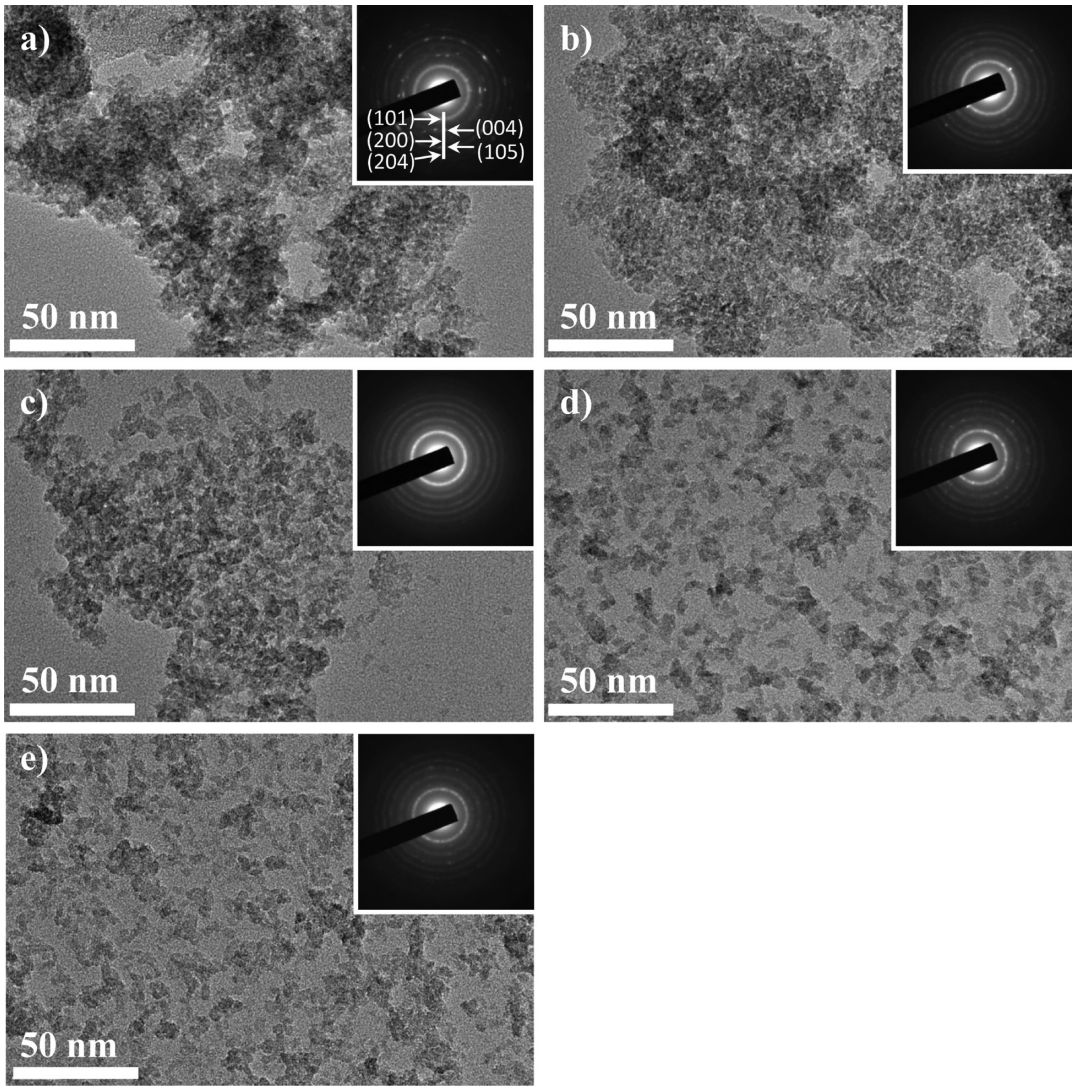

Figure 6. TEM micrographs of room-temperature-synthesized samples with (a) 0, (b) 0.5, (c) 1, (d) 2.5, and (e) 5% Fe^{3+}. SAED pattern attribution corresponds to the anatase polymorph.

Table 3. Comparison between the Theoretical and Measured Values or Iron Concentration by EDX and ICP-AES in the Doped TiO_2 Materials

nominal [Fe] atom % in solution	0.5	1	2.5	5
EDX [Fe] atom %	0.8	2.3	4.2	7
ICP-AES [Fe] atom %	0.45	2.1	4.2	7.7

have reported that trivalent doping in TiO_2 has no or very little influence on the electronic conductivity. We can hypothesize that the point defect introduced by the inclusion of Fe^{3+} in the lattice and the underlying formation of oxygen vacancies contribute to some extent to promoting faster lithium mobility in the crystal structure.

In recharge, a fairly similar trend is observed, namely, an increase in the charge capacity at $C/2$, a less blatant change at $C/20$, and no effect at the $C/50$ regime. For the latter, a heavily doped 5% material even shows lower charge capacity than TiO_2 (Figure 8c).

These results underline that a low iron doping level in the nanocrystalline anatase TiO_2 is beneficial to reaching a gravimetric capacity closer to the theoretical value, especially at medium/high regimes. This is not only true for the first cycles, but this trend is at least maintained over 50 cycles at $C/2$ rate (Figure 9). For undoped and a 0.5% doping level, the Coulombic efficiency is maintained over 99.5% after 10 cycles; heavier doping levels are found to harm the Coulombic efficiency, thus explaining the crossover in the gravimetric capacity at around 50 cycles.

The origin of the extra-capacity in discharge for doping of TiO_2 with iron remains relatively equivocal. Das et al. have hypothesized the conversion reaction to be responsible of this extra-capacity once the $Li_{1.0}TiO_2$ composition is reached.[47] Although the conversion reaction is particularly well supported on their materials discharged to 0.005 V, such a reaction taking place at potentials above 1 V remains astonishing. The authors have also not clearly commented the huge capacity difference between TiO_2 (620 mAh/g) and iron-doped TiO_2 (>1300 mAh/g) at a discharge potential of 0.005 V, which could not account for a simple conversion reaction. To achieve better insight on the origin of this extra-capacity observed above 1 V (vs Li^+/Li), HRTEM analysis on discharged samples was realized. SAED patterns recorded on the different samples (TiO_2, 2.5% and 5% doped TiO_2) did not show the presence of titanium or iron metal particles, enabling us to verify that the

dx.doi.org/10.1021/ic501067p | Inorg. Chem. 2014, 53, 10129−10139

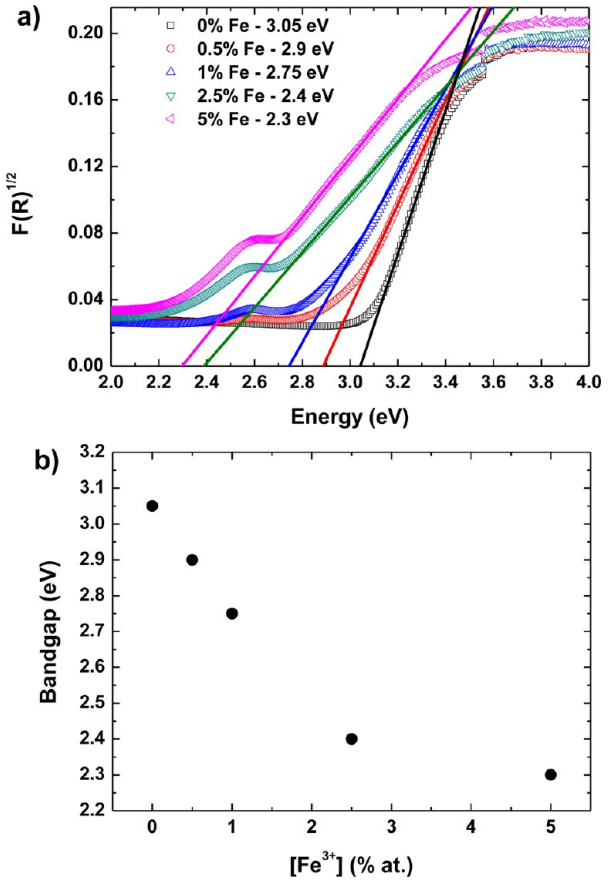

Figure 7. (a) UV−vis absorption spectra of synthesized particles with different Fe^{3+} concentrations. (b) Corresponding band-gap values. $F(R)$ is the Kubelka−Munk function.

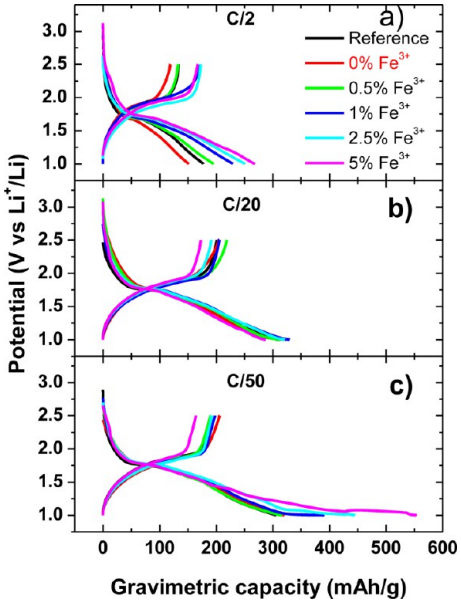

Figure 8. First charge/discharge profile recorded at (a) $C/2$, (b) $C/20$, and (c) $C/50$ corresponding to room-temperature-synthesized anatase TiO_2 at pH = 2 (0% Fe^{3+}) and pH = 3 (reference) and iron-doped TiO_2 synthesized at pH = 2 using different iron concentrations.

conversion reaction does not take place at above 1 V. The structure of the particles agrees with the tetragonal $LiTiO_2$ rock-salt crystal structure. The original Fe^{3+} valence state turns

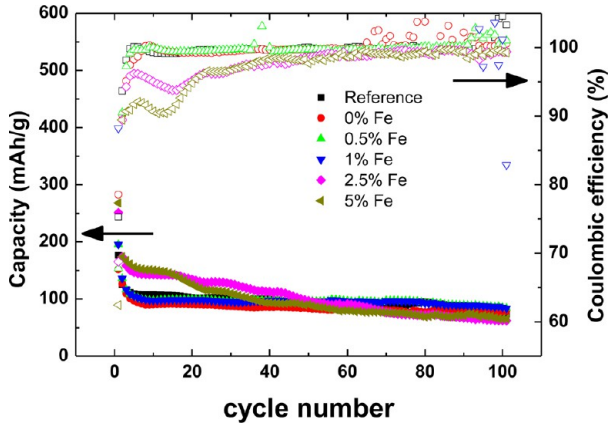

Figure 9. Gravimetric capacity retention of room-temperature-synthesized anatase TiO_2 at pH = 2 (0% Fe^{3+}) and pH = 3 (reference) and iron-doped TiO_2 synthesized at pH = 2 using different iron concentrations (iron-doped) at $C/2$.

to a partial reduction onto Fe^{2+}, as suggested electron energy loss spectroscopy (EELS) measurements on electrochemically discharged samples (Figure S4 in the SI). The main difference arises from the formation of an electrolyte degradation layer, whose thickness increases with the doping level to reach a thickness of a few nanometers (Figure 10). Although the slight morphological modifications induced by iron doping could contribute to some extent to the evolution of the electrochemical characteristics of the electrode, the large difference experienced between the samples emphasizes the role played by iron doping, which, on the one hand, has a beneficial effect to obtain higher rate capability but, on the other hand, catalyzes the electrolyte degradation at potentials of around 1 V, thus giving a more robust explanation on the extra-capacity apparition observed not only in this work but also by Das et al.[47]

b. Photocatalysis Characteristics for RhB Photodegradation. Taking advantage of the band-gap shift to the visible range, from 400 to 540 nm, and the high surface area of the particles favorable for ensuring an extended interface for interfacial photon-induced charge-transfer processes, the second application investigated in this work concerns evaluation of the photocatalytic activity of the semiconductors with respect to the photodegradation of RhB. For this, to mimic the most outdoor conditions, the photodegradation of RhB was evaluated under white-light excitation by means of a 3A quality xenon light source adapted to global AM1.5G conditions (P_{ill} = 1000 W/m^2). For appropriate evaluation of the real dopant effect, the photoactivity of the doped materials is compared to that of the undoped counterpart used as a benchmark.

RhB is a typical fluorescent marker dye exhibiting absorbance at ca. 550 nm, resulting in intramolecular $\pi-\pi^*$ transitions, and long-lived fluorescence, exhibiting slight Stokes shift of ca. 50 nm with a quantum yield of 65% in basic ethanol.[51]

Figure 11 summarizes the evolution of the UV−vis absorption spectrum of RhB as a function of the illumination time. The progress of RhB photodegradation is visually monitored by the bleaching of the solution, which translates to a loss of absorbance and a hypsochromic shift of the 552 nm band. This optical evolution stems from the stepwise removal of the ethyl units on the amine part of the dye.[52,53] The mechanism of degradation thus involves a first ethyl elimination shifting the absorption to 539 nm and a second continuing the

dx.doi.org/10.1021/ic501067p | Inorg. Chem. 2014, 53, 10129−10139

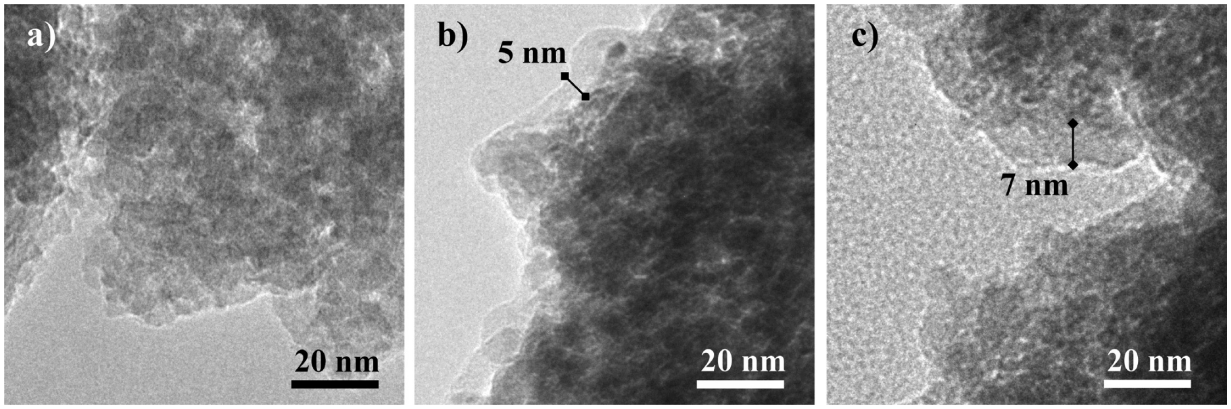

Figure 10. TEM micrographs of samples retrieved after a first discharge at C/50: (a) 0% Fe^{3+}; (b) 2.5% Fe^{3+}; and (c) 5% Fe^{3+}.

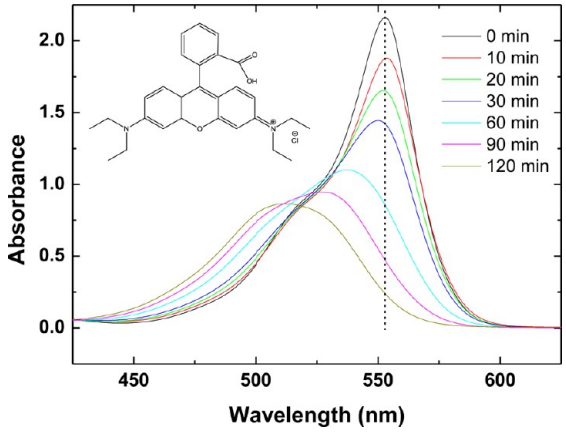

Figure 11. Evolution of the UV−vis spectrum of a RhB solution as a function of the illumination time.

hypsochromic shift to 522, 510, and finally 480 nm for the dye completely de-ethylated.

The RhB photodegradation as a function of time is reported in Figure 12 including error bars deduced from the reproduction of the experiments. Besides, for the undoped and 0.5% doped TiO_2, for which the catalytic activity slows down after 1 h of illumination (and 90 min respectively), the linear relationship between $\ln(C/C_0)$ and time highlights that the photocatalytic degradation of RhB is a first-order kinetic

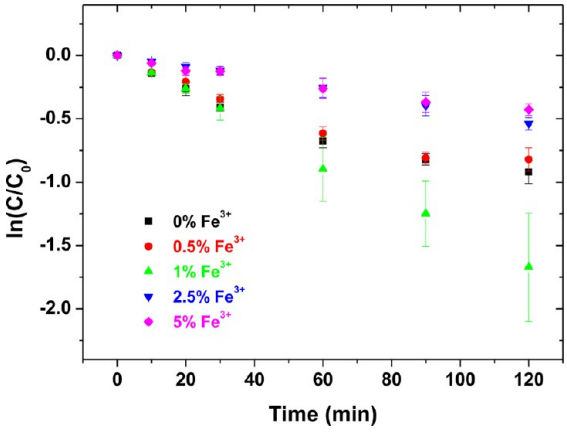

Figure 12. Evolution of the $\ln(C/C_0)$ as a function of time for different concentrations of Fe^{3+} in TiO_2.

from which the slope leads to the degradation rate constant (k_{deg}). The values of k_{deg} for the different materials are reported in Table 4. Note that, for undoped TiO_2 and the 0.5% doped

Table 4. Evolution of the RhB Degradation Rate Constant for TiO_2 and Fe-Doped TiO_2 at Different Levels

nominal [Fe] atom % in solution	0	0.5	1	2.5	5
k (min^{-1})	0.0112	0.0094	0.0111	0.0045	0.0030

samples, a nonlinear behavior is observed after 60 and 90 min, respectively. Although actually this phenomenon is not clearly understood, it is a feature also observed by other groups when using TiO_2 and white-light illumination.[54]

Our results confirm a beneficial effect of doping by iron for white-light excitation as long as the material contains low iron concentration levels. The best performances are obtained for 1% Fe-TiO_2, which allows after 2 h of illumination photodegradation of as high as 73% of the initial RhB (Figure 13).

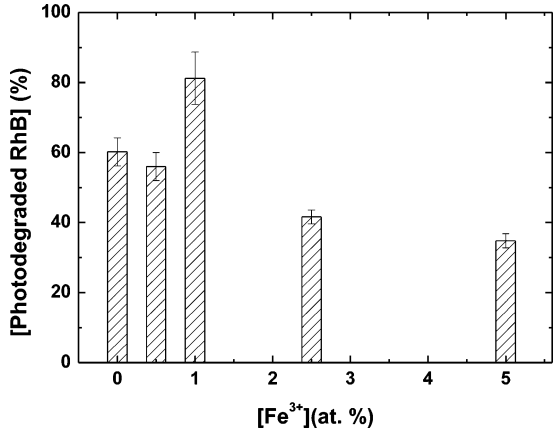

Figure 13. Evolution of the concentration of RhB photodegraded in 120 min by undoped TiO_2 and different levels of iron-doped TiO_2.

For lower iron concentration, the photodegradation yield is in the range of 59%, whereas for higher iron concentration, the yield decreases markedly to 41% and even to 31% for 5% Fe^{3+} in spite of the greater visible-light absorption of these materials. The degradation mechanism of RhB involves the band-gap excitation of TiO_2, leading to e^-/h^+ dissociation. The electron promoted to the conduction band is scavenged by chemisorbed oxygen to form the strong oxidative $O_2^{\bullet-}$ species that in a

dx.doi.org/10.1021/ic501067p | Inorg. Chem. 2014, 53, 10129−10139

second step will react with H^+ to form H_2O_2. On the other hand, the hole located in the valence band, which has strong O 2p character, will react with water to form $OH^•$, which will directly oxidize the rhodamine. The decrease of the photocatalytic activity for a high concentration of dopant can thus be attributed to the lower charge-separation lifetime.[55] Indeed, increasing excessively the dopant concentration in the anatase will induce the creation of defect levels within the band-gap, thus increasing the probability of a recombination event of the electron−hole pairs. This trade-off is often encountered in the photoelectrochemical system, especially when the charge-carrier concentration becomes too high, limiting the carrier diffusion length. Only very few works related to the photodegradation of RhB using white light are reported in the literature, and no rate constant obtained in comparable experimental conditions has been found.

CONCLUSIONS

A high range of iron-doped nanocrystalline TiO_2 particles have been successfully synthesized using a room-temperature approach by means of controlling the pH of the aging solution and utilizing an adequate type of precursor. The mechanism of crystallization from $Ti(OH)_4$ to the anatase TiO_2 is ascribed to a dissolution/crystallization process involving the incorporation of iron during the polycondensation process. The incorporation of up to 7.7 atom % of Fe^{3+} in the anatase lattice is achieved, underlining against the general preconceived idea that a high temperature for synthesis and doping is needed for the introduction of a quantitative amount of dopant. This work is an additional example demonstrating the potentialities of room-temperature synthesis that falls within the topic of the development of greener chemistry. The particles prepared by this very soft method exhibit a high surface area from 260 to 280 m^2/g, a particle size in the range of 5−6 nm, and a band-gap narrowing from 3.05 to 2.3 eV, rendering the coloration of the particles orange and thus photoactive in the visible portion of the solar spectrum. These particles were successfully introduced into lithium-ion batteries. Their electrochemical behavior points out a noticeable improvement by doping with iron in terms of charge/discharge gravimetric capacity especially at moderate and high cycling rates. By contrast, too high iron doping harms the Coulombic efficiency, and the presence of iron in the anatase lattice catalyzes electrolyte degradation at potentials between 1 and 1.5 V for a low charge/discharge rate ($C/50$). Finally, the photocatalytic activity of our particles with respect to RhB degradation was also investigated using a standard illumination procedure, inspired from solar PV (AM1.5G conditions). As for the batteries, a trade-off dopant concentration is experienced to combine high visible-light absorption and long charge-separation lifetime. The best results were obtained with low doping level, namely, 1% Fe-doped TiO_2, for which, after 120 min of irradiation, more than 73% RhB was degraded.

ASSOCIATED CONTENT

Supporting Information

X-ray diffractogram of undoped samples, XRD patterns, and an EELS spectrum. This material is available free of charge via the Internet at http://pubs.acs.org.

AUTHOR INFORMATION

Corresponding Author

*E-mail: frederic.sauvage@u-picardie.fr. Phone: +33 3 2282 7971.

Notes

The authors declare no competing financial interest.

ACKNOWLEDGMENTS

C.A. is indebted to the ANR Labex "Store-ex" for funding. The authors thank Dr. Sophie Cassaignon (LCMCP), Prof. Lorenzo Stievano (ICGm), and Dr. Nadia Barbero (LRCS) for fruitful discussions and the Electron Microscopy Platform of IMPC (Institut des Matériaux de Paris Centre FR2482) for their contributions.

REFERENCES

(1) Deshpande, S. B.; Potdar, H. S.; Khollam, Y. B.; Patil, K. R.; Pasricha, R.; Jacob, N. E. *Mater. Chem. Phys.* **2006**, *97*, 207.
(2) Hegazy, A.; Prouzet, E. *Chem. Mater.* **2012**, *24*, 245.
(3) Sauvage, F.; Bodenez, V.; Tarascon, J.-M.; Poeppelmeier, K. R. *J. Am. Chem. Soc.* **2010**, *132*, 6778.
(4) Albrecht, T. A.; Sauvage, F.; Bodenez, V.; Tarascon, J.-M.; Poeppelmeier, K. R. *Chem. Mater.* **2009**, *21*, 3017.
(5) Jung, H.-G.; Yoon, C. S.; Prakash, J.; Sun, Y.-K. *J. Phys. Chem. C* **2009**, *113*, 21258.
(6) Klosek, S.; Raftery, D. *J. Phys. Chem. B* **2001**, *105*, 2815.
(7) Cengiz, E.; Wissing, S. A.; Müller, R. H.; Yazan, Y. *Int. J. Cosmet. Sci.* **2006**, *28*, 371.
(8) Reck, E.; Seymour, S. *Macromol. Symp.* **2002**, *187*, 707.
(9) Linsebigler, A. L.; Lu, G.; Yates, J. T., Jr. *Chem. Rev.* **1995**, *95*, 735.
(10) Hardin, B. E.; Snaith, H. J.; McGehee, M. G. *Nat. Photonics* **2012**, *6*, 162.
(11) Su, X.; Wu, Q.; Zhan, X.; Wu, J.; Wei, S.; Guo, Z. *J. Mater. Sci.* **2012**, *47*, 2519.
(12) Chen, X.; Liu, L.; Yu, P. Y.; Mao, S. S. *Science* **2011**, *331*, 746.
(13) Naldoni, A.; Allieta, M.; Santangelo, S.; Marelli, M.; Fabbri, F.; Cappeli, S.; Bianchi, C. L.; Psaro, R.; Santo, V. D. *J. Am. Chem. Soc.* **2012**, *134*, 7600.
(14) Satoh, N.; Nakashima, T.; Kamikura, K.; Yamamoto, K. *Nat. Nanotechnol.* **2008**, *3*, 106.
(15) Patra, S.; Davoisne, C.; Bruyère, S.; Bouyanfif, H.; Cassaignon, S.; Taberna, P.-L.; Sauvage, F. *Part. Part. Syst. Charact.* **2013**, *30*, 1093.
(16) Wagemaker, M.; Borghols, W. J. H.; van Eck, E. R. H.; Kentgens, A. P. M.; Kearley, G. J.; Mulder, F. M. *Chem.—Eur. J.* **2007**, *13*, 2023.
(17) Gentili, V.; Brutti, S.; Hardwick, L. J.; Armstrong, A. R.; Panero, S.; Bruce, P. G. *Chem. Mater.* **2012**, *24*, 4468.
(18) Kim, H.; Kim, M. G.; Cho, J. *Adv. Energy Mater.* **2012**, *2*, 1425.
(19) Shannon, R. D. *Acta Crystallogr.* **1976**, *A32*, 751.
(20) Kubelka, P.; Munk, F. *Z. Technol. Phys. (Liepzig)* **1931**, *12*, 593−601.
(21) Spurr, R. A.; Myers, H. *Anal. Chem.* **1957**, *29*, 760−762.
(22) Durupthy, O.; Bill, J.; Aldinger, F. *Cryst. Growth Des.* **2007**, *7*, 2696.
(23) Schott, J.; Pokrovsky, O. S.; Oelkers, E. H. *Rev. Mineral. Geochem.* **2009**, *70*, 207−258.
(24) Gopal, M.; Chan, W. J. M.; De Jonghe, L. C. *J. Mater. Sci.* **1997**, *32*, 6001.
(25) Sugimoto, T.; Zhou, X.; Muramatsu, A. *J. Colloid Interface Sci.* **2003**, *259*, 43.
(26) Dambournet, D.; Belharouak, I.; Amine, K. *Chem. Mater.* **2010**, *22*, 1173.
(27) Sugimoto, T.; Zhou, X.; Muramatsu, A. *J. Colloid Interface Sci.* **2002**, *252*, 339.
(28) Stefansson, A. *Environ. Sci. Technol.* **2007**, *41*, 6117.
(29) Flyn, C. M., Jr. *Chem. Rev.* **1984**, *84*, 31.

(30) Ruiz, A. M.; Dezanneau, G.; Arbiol, J.; Cornet, A.; Morante, J. R. *Chem. Mater.* **2004**, *16*, 862.
(31) Chandiran, A. K.; Sauvage, F.; Casas-Cabanas, M.; Comte, P.; Zakeeruddin, S. M.; Gräetzel, M. *J. Phys. Chem. C* **2010**, *114*, 15849.
(32) Chandiran, A. K.; Sauvage, F.; Etgar, L.; Gräetzel, M. *J. Phys. Chem. C* **2011**, *115*, 9232.
(33) Wang, J. A.; Limas-Ballesteros, R.; Lopez, T.; Moreno, A.; Gomez, R.; Novaro, O.; Bokhimi, X. *J. Phys. Chem. B* **2001**, *105*, 9692.
(34) Schwertmann, U.; Friedl, J.; Pfab, G.; Gehring, A. U. *Clays Clay Miner.* **1995**, *43*, 599.
(35) Patel, S. K. S.; Kurian, S.; Gajbhiye, N. S. *AIP Adv.* **2012**, *2*, 012107.
(36) Rodriguez-Torres, C. E.; Cabrera, A. F.; Errico, L. A.; Adan, C.; Requejo, F. G.; Weissmann, M.; Stewart, S. J. *J. Phys.: Condens. Matter* **2008**, *20*, 135210.
(37) Lee, H. M.; Kim, S. J.; Shim, I.-B.; kim, C. S. *IEEE Trans. Magn.* **2003**, *39*, 2788.
(38) Hirano, M.; Joji, T.; Inagaki, M.; Iwata, H. *J. Am. Ceram. Soc.* **2004**, *87*, 35.
(39) Wang, C.-Y.; Böttcher, C.; Bahnemann, D. W.; Dohrmann, J. K. *J. Mater. Chem.* **2003**, *9*, 2322.
(40) Wang, X. H.; Li, J.-G.; Kamiyama, H.; Katada, M.; Ohashi, N.; Moriyoshi, Y.; Ishigaki, T. *J. Am. Chem. Soc.* **2005**, *127*, 10982.
(41) Sanchez, E.; Lopez, T. *Mater. Lett.* **1995**, *25*, 271.
(42) Smith, G.; Halenius, U.; Annersten, H.; Ackermann, L. *Am. Mineral.* **1983**, *68*, 759.
(43) Baudrin, E.; Cassaignon, S.; Koelsch, M.; Jolivet, J.-P.; Dupont, L.; Tarascon, J.-M. *Electrochem. Commun.* **2007**, *9*, 337.
(44) Johnson, W. C. *Acta Mater.* **2001**, *49*, 3463.
(45) Cava, R. J.; Murphy, D. W.; Zahurak, S.; Santoro, A.; Roth, R. S. *J. Solid State Chem.* **1984**, *53*, 64.
(46) Lafont, U.; Carta, D.; Mountjoy, G.; Chadwick, A. V.; Kelder, E. M. *J. Phys. Chem. C* **2010**, *114*, 1372.
(47) Das, S. K.; Gnanavel, M.; Patel, M. U. M.; Shivakumara, C.; Bhattacharyya, A. J. *J. Electrochem. Soc.* **2011**, *158*, A1290.
(48) Poizot, P.; Laruelle, S.; Grugeon, S.; Dupont, L.; Tarascon, J.-M. *Nature* **2000**, *407*, 496−499.
(49) Hutchings, G. S.; Liu, Q.; Jiao, F. *J. Electrochem. Soc.* **2013**, *160*, A511.
(50) Kyerematen, N. A.; Hornebecq, V.; Martinez, H.; Knauth, P.; Djenizian, T. *ChemPhysChem* **2012**, *13*, 3707−3713.
(51) Kubin, R. F.; Fletcher, A. N. *J. Lumin.* **1982**, *27*, 455.
(52) Fu, H.; Pan, C.; Yao, W.; Zhu, Y. *J. Phys. Chem. B* **2005**, *109*, 22432.
(53) Wu, T.; Liu, G.; Zhao, J.; Hidaka, H.; Serpone, N. *J. Phys. Chem. B* **1998**, *102*, 5845.
(54) Siravanjani, K.; Gopinath, C. S. *J. Mater. Chem.* **2011**, *21*, 2639.
(55) Choi, W.; Termin, A.; Hoffmann, M. R. *J. Phys. Chem.* **1994**, *98*, 13669.